AIAA 2000-3722
Flow Analysis of X-34 Main Propulsion System Feedlines

B. Vu and R. Garcia
NASA Marshall Space Flight Center
Huntsville, AL

36th AIAA/ASME/SAE/ASEE
Joint Propulsion Conference
17–19 July 2000
Huntsville, Alabama

Flow Analysis of X-34 Main Propulsion System Feedlines

B. T. Vu* and R. Garcia†
NASA Marshall Space Flight Center, Huntsville, AL 35812

Abstract

The X-34 Main Propulsion System (MPS) configuration includes the liquid oxygen (LOX) and rocket propellant #1 (RP-1) feedlines (Figure 1) The flow analyses of these feedlines were performed and documented in previous studies [1]. These analyses predicted a relatively low inlet distortion and nearly even flow split at the engine interface. The new design for these MPS feedlines has been recommended recently. The new configuration includes a tighter radius in the RP-1 feedline and a neck-down section between the gimbals (Figure 2). Conversely, the LOX feedline is very similar to the previous design. There were concerns that this new RP-1 configuration might generate a greater flow distortion at the engine interface than the original design. To resolve this issue, a Computation Fluid Dynamics (CFD) analysis was conducted to determine the flow field in the new RP-1 feedlines.

Introduction

The flow field at the engine interface can have a large effect on pump performance and structural integrity. Distorted flow at the pump inlet can lead to significant decreases in suction capability and head rise as well as unacceptably high dynamic loads. Because of this CFD analyses have been performed for the LOX and RP-1 feedlines.

This paper describes the procedure to obtain the flow field in the RP-1 feedline and reports the predicted environments at the engine interface as well as the simplifications and assumptions embedded in the analyses. The flow analyses of the new LOX feedline configuration will be included in the full paper.

Modeling

A model was created and analyses were performed on the new design of the MPS feedlines. The new analyses included the pressure-compensated bellow, which for simplification was disregarded in previous analyses. Figure 3 shows the configurations of both designs. The new design, shown in wireframe, is overlaid on top of the old design. Note that the model does not include the gimbal joints, fuel filters, and flow meters. The computational domain for the new design included 3 blocks with a total of 239,463 grid points. The grids were generated using the code GRIDGEN [1]. The solutions were obtained using the code FDNS [2], a three-dimensional Navier-Stokes flow solver, with a κ–ε turbulence model. The analyses performed were single phase, incompressible, and steady state. Fully developed velocity and turbulence profiles were used at the inlet and mass conservation was enforced at the exit. At the pipe surfaces, no-slip wall boundary conditions were applied. The flow fields were initialized to the reference conditions, which are listed in Table 1.

Table 1. RP-1 Reference Conditions

mass flow (lbm/sec)	64.29
reference pressure (psi)	37
reference temperature (°R)	530
reference density (lmb/ft^3)	50.3
Reynolds number	2.4 x 10^5

Numerical Methodology

The basic equations employed to describe the MPS feedline flow field are the multidimensional, general coordinate transport equations. A generalized form of these equations written in curvilinear coordinates is given by

$$(1/J)(\partial\rho q/\partial t) = \partial[-\rho U_i q + \mu G_{ij}(\partial q/\partial\xi_j)]/\partial\xi_i + (1/J)S_q$$

where J, Ui and G_{ij} are written as:

$$J = \partial(\xi_i\xi_j)/\partial(x,y)$$

$$Ui = (u_j/J)(\partial\xi_i/\partial x_j)$$

$$G_{ij} = (\partial\xi_i/\partial x_k)(\partial\xi_j/\partial x_k)/J,$$

where q represents 1, u, v, w, h, k, and ε, respectively. These are equations of continuity, x, y, and z momentum, enthalpy, turbulent kinetic energy, and turbulent kinetic energy dissipation rate. ξ is the transformed curvilinear coordinate. $\mu = (\mu_l+\mu_t)/\sigma_q$ is the effective viscosity when the turbulent eddy viscosity concept is employed to model the turbulent flows. is the laminar viscosity; $\mu_t=\rho C_\mu k^2/\varepsilon$, is the turbulence eddy

Submitted to the AIAA 36th Joint Propulsion Conference and Exhibit, Huntsville, AL, July 16-19, 2000.

* Aerospace Engineer, Applied Fluid Dynamics, MSFC, AL, Member AIAA
† Group Leader, Applied Fluid Dynamics, MSFC, AL, Member AIAA

viscosity and C_μ and σ_q denote turbulence modeling constants. Turbulence modeling constants σ_q and source terms S_q are given in Table 2.

ϕ is the energy dissipation function and P_r represents the turbulent kinetic energy production term. C_1, C_2, and C_3 are model constants for the two-equation turbulence models.

Table 2. σ_q and S_q of the Transport Equations

q	σ_q	S_q
1	1.00	0
u	1.00	$-p_x + \nabla[\mu(u_j)_x] - 2/3(\mu\nabla u_j)_x$
v	1.00	$-p_y + \nabla[\mu(u_j)_y] - 2/3(\mu\nabla u_j)_y$
w	1.00	$-p_z + \nabla[\mu(u_j)_z] - 2/3(\mu\nabla u_j)_z$
h	0.95	$Dp/Dt + \phi$
k	0.89	$\rho(P_r-\varepsilon)$
ε	1.15	$\rho(\varepsilon/k)(C_1P_r - C_2\varepsilon + C_3P_r^2/\varepsilon)$

To solve the system of nonlinear, coupled partial differential equations, finite difference approximations are used to establish a system of linearized algebraic equations. A relaxation solution procedure is then employed to couple the equations. An adaptive upwind scheme is employed to approximate the convective terms of the momentum, energy and continuity equations; the scheme is based on second- and fourth-order central differencing with artificial dissipation. First-order upwinding is used for species and turbulence equations since the parameters involved are positive quantities. Different eigenvalues are used for weighting the dissipation terms depending on the conserved quantity being evaluated in order to give correct diffusion fluxes near wall boundaries. Details of the present numerical methodology is given in [4, 5].

Discussion of Results

The velocity profile just inside the pipe surface is shown in Figure 4. The flow separation can be seen only at the stagnation pocket to the right of the pressure-compensated bellow. Also, there is flow acceleration and deceleration through the elbows and neck-down regions. The close-up views of velocity vectors (Figure 5) show the recirculation zones in the stagnation region, flow accelerations and decelerations over the bends, and uniform flow at the engine interface. A comparison of the velocity profiles along mutually perpendicular directions of the duct cross-section shows comparable velocity distortions at the engine interface for the new and the old designs (Figure 6). A more complete description of the flow field at the engine interface can be seen in the velocity contour plots for both designs (Figure 7). As seen in these plots, the new design indicates less flow variations at the engine interface.

Figure 8 shows the static pressure on the pipe surface. These pressures are scaled to the reference pressure (37 psi) at the engine interface. As expected, the bends generated pressure gradients normal to the bend radius, i.e. the pressure is low on the inner radius and higher on the outer radius of the elbow. The mass-averaged pressure distribution along the feedline model and its resulting pressure coefficients are shown in Figure 9 and Figure 10, respectively. Note that the elbows generated the secondary flows, which eventually contributed to the pressure losses, as seen in the pressure plots. The pressure drop between the inlet and the engine interface is about 4.6 psi for the new design, compared to 4.1 psi in the previous design. However, this number may not be accurate since the model does not include the gimbal joints, fuel filters, and flow meters. These features are expected to have an impact on the pressure drop, but not much on the flow profiles.

Conclusions

In conclusion, the analyses indicate that the new duct design does not have a significant affect on the flow at the outlet of the feedline. It is also shown that the flow development is more favorable in the new design, although the pressure drop is slightly higher in this design. The introduction of the neck-down and the tighter bend did not grossly affect the flow and since the flow is fully developed at the engine interface, there is no need to use the flow straighteners at the engine inlet.

References

1. Garcia, R., "X-34 CFD Feedlines Analysis Results," X-34 CDR, Marshall Space Flight Center, Dec. 15-17, 1997.
2. Steinbrenner, J.P., Chawner, J.R., and Fouts, C.L., "The GRIDGEN3D Multiple Block Grid Generation System, Vol. I and II," General Dynamics Corp, Fort Worth, Texas, July 1990.
3. Chen, Y.S., "FDNS, A General Purpose CFD Code, User's Guide, version 3.0," Engineering Sciences, Inc., May 1, 1993.
4. Wang, T.S., "Numerical Study of the Transient Nozzle Flow Separation of Liquid Rocket Engines," Computational Fluid Dynamics Journal, Vol. 1(3), pp. 305-314, 1992.
5. Wang, T.S. and Chen, Y.S., "Unified Navier-Stokes Flowfield and Performance Analysis of Liquid Rocket Engines, J. Propulsion Power," Vol. 9(5), pp. 678-685, 1993.

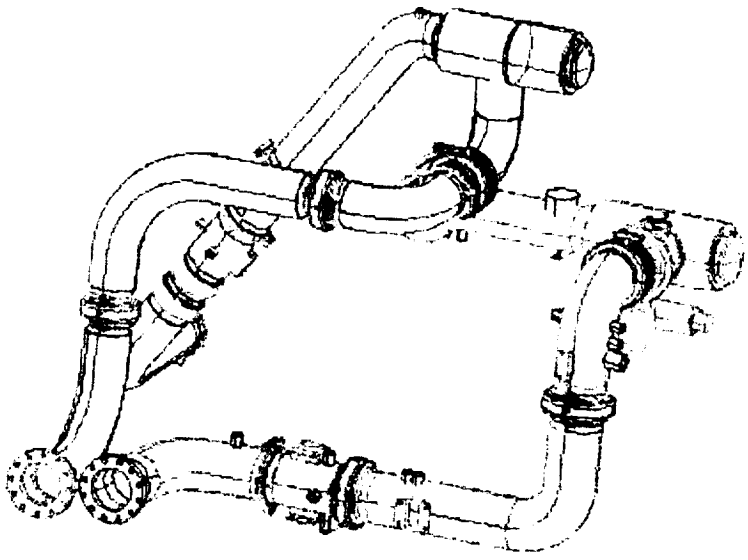

Figure 1: X-34 MPS Feedlines (Old Design)

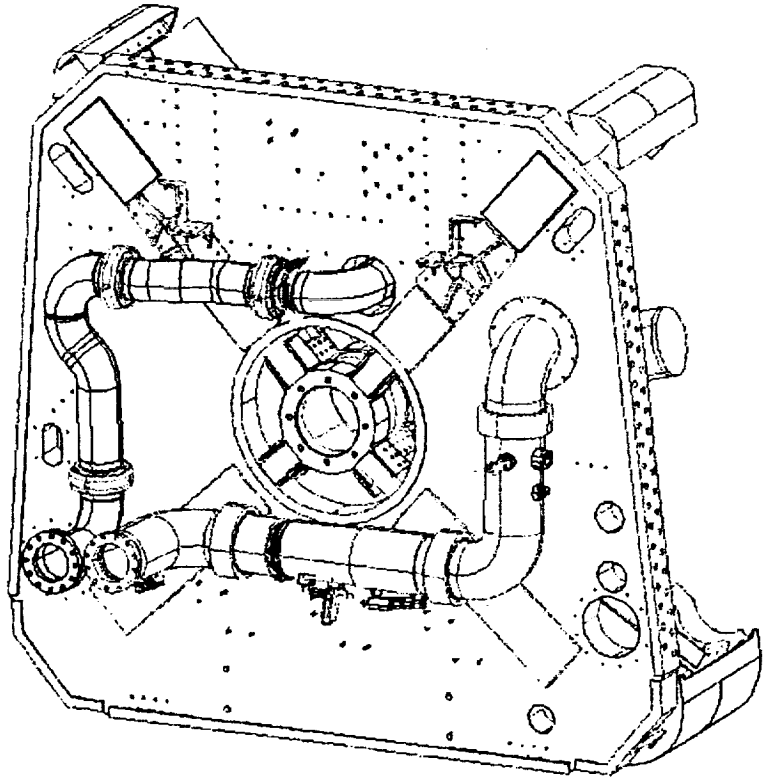

Figure 2: X-34 MPS Feedlines (New Design)

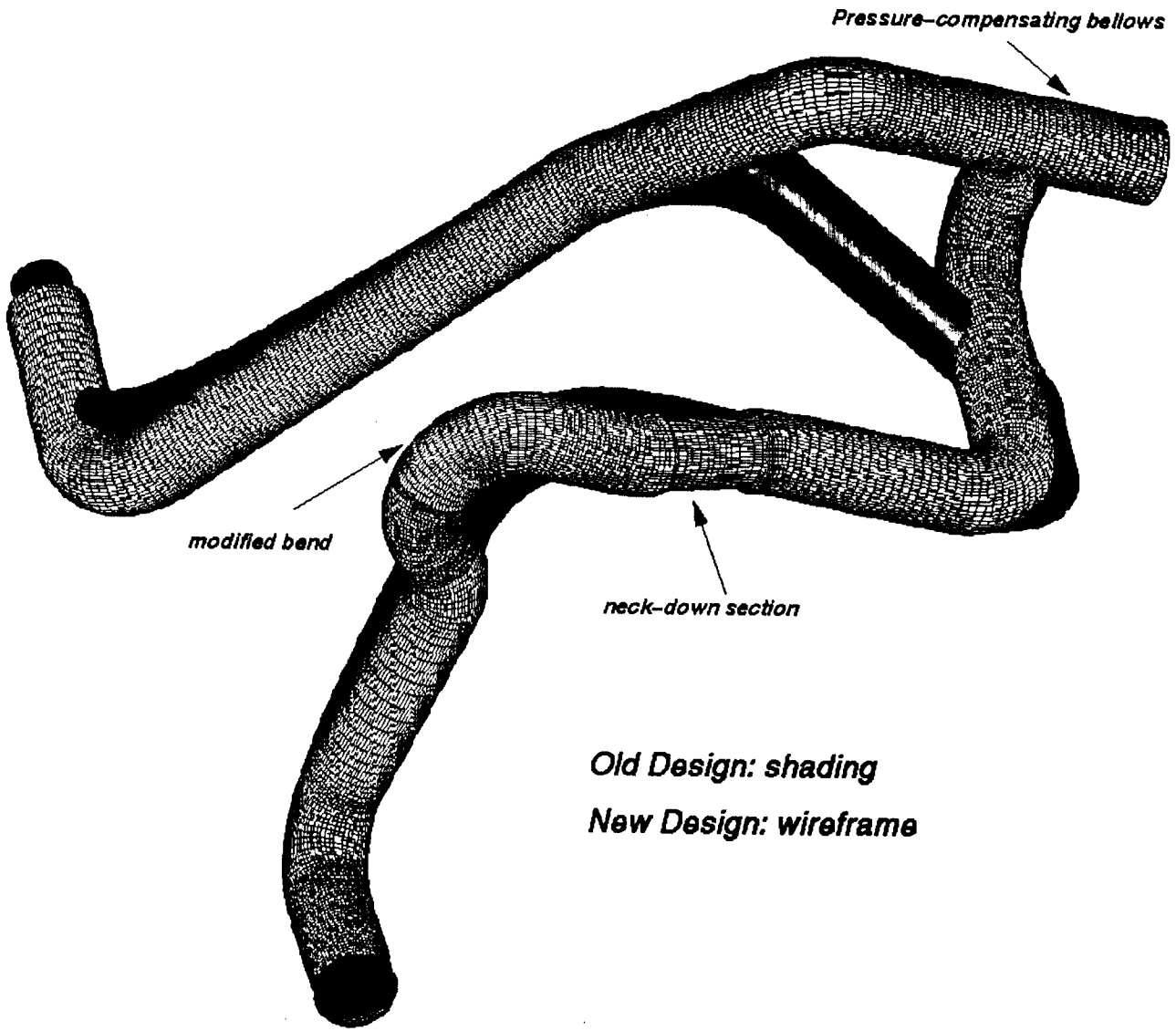

Figure 3: Old vs. New Design

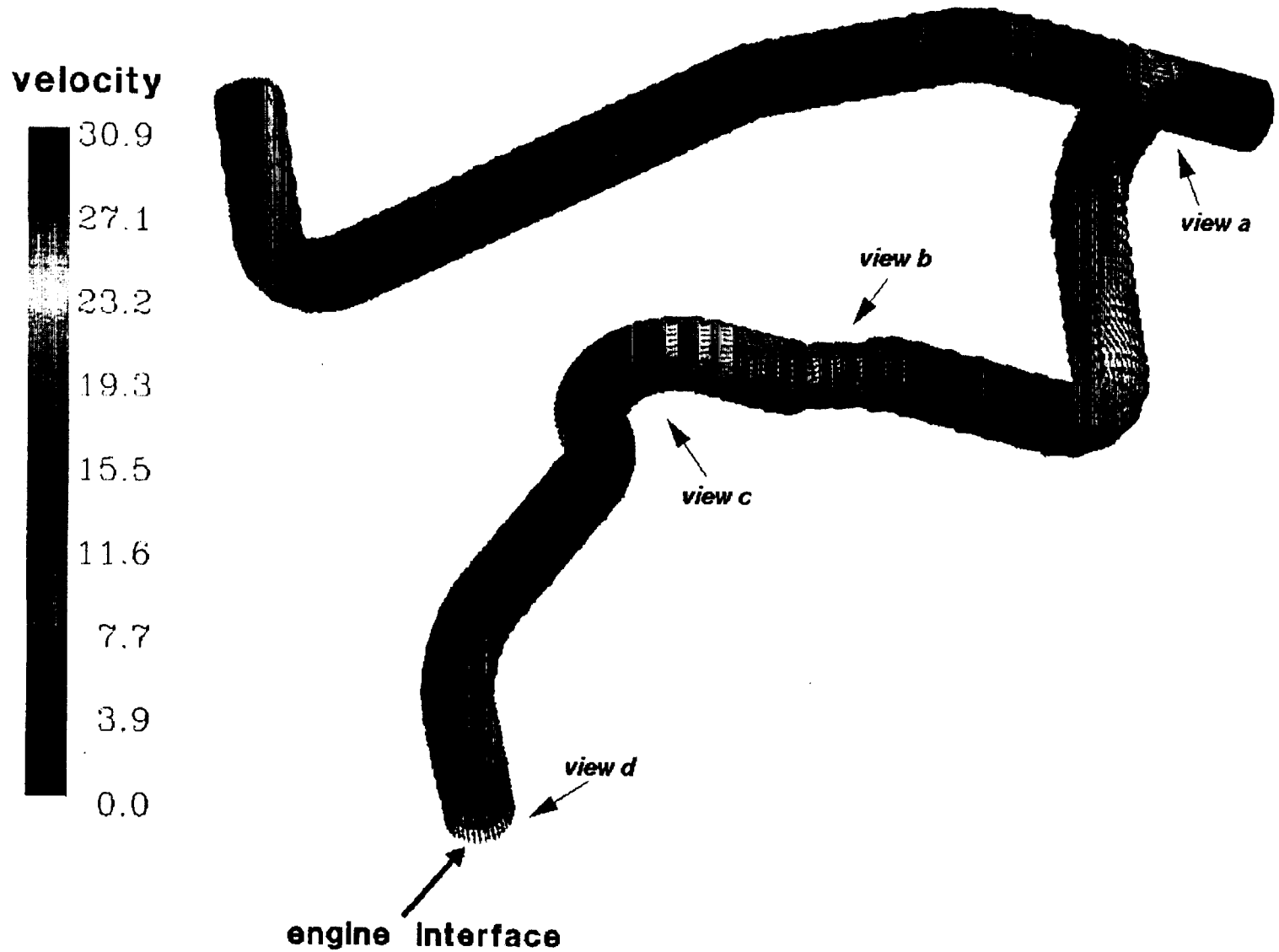

Figure 4: Velocity Magnitude and Vectors for the RP-1 Feedline

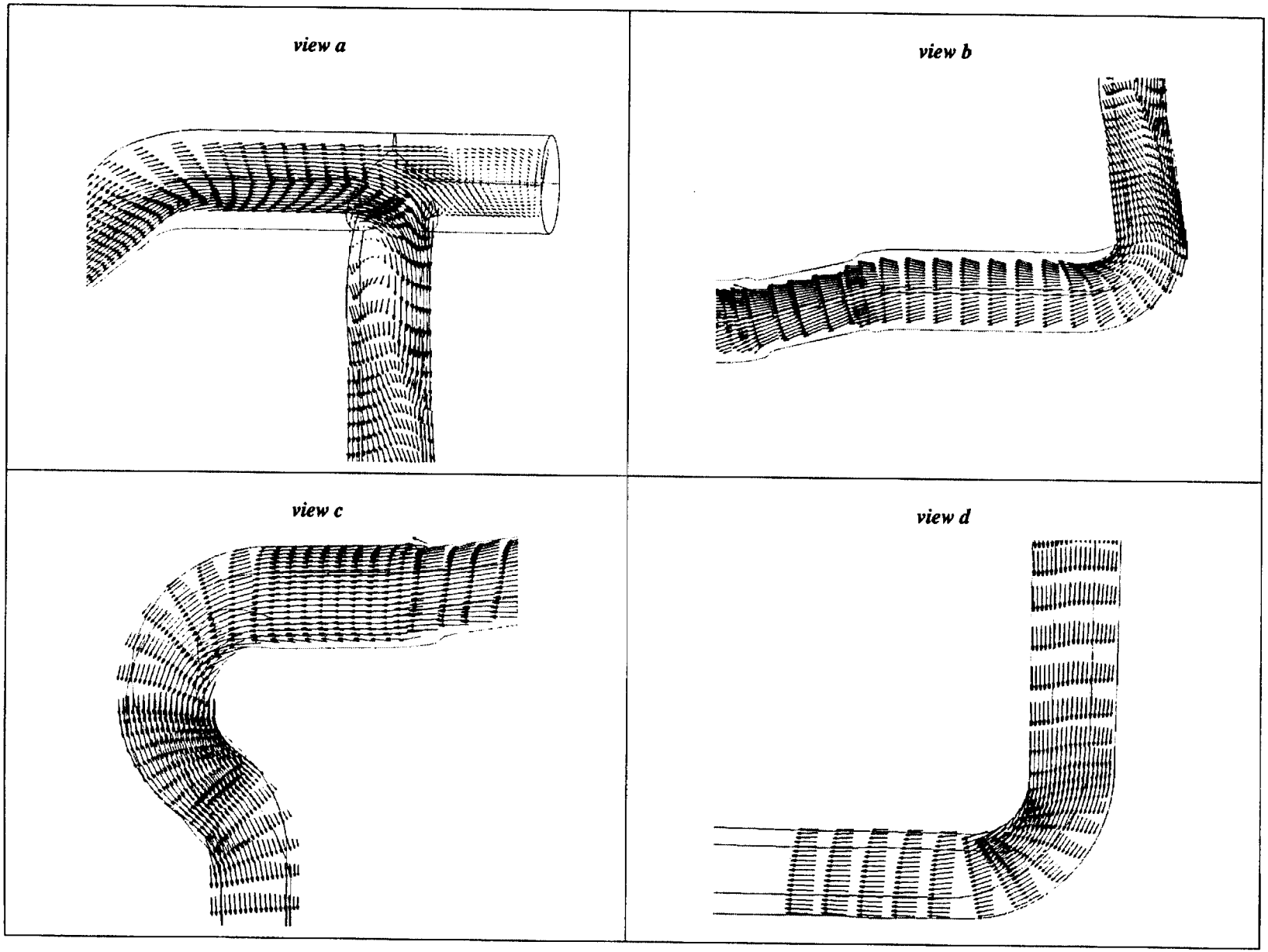

Figure 5: Velocity Vectors (close-up view)

X-34 RP-1 Feedline CFD Results

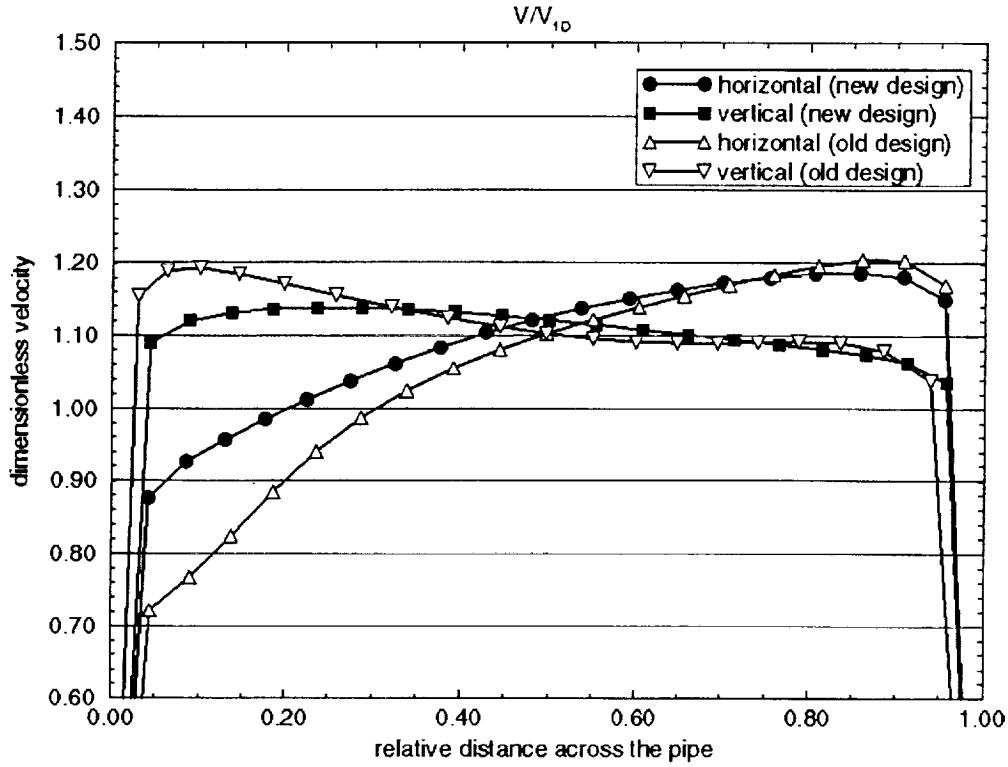

Figure 6: Velocity Profiles at the Engine Interface

RP-1 Feedline CFD Results: Orbital's Design

Nondimensionalized Axial Velocity at the Engine Interface

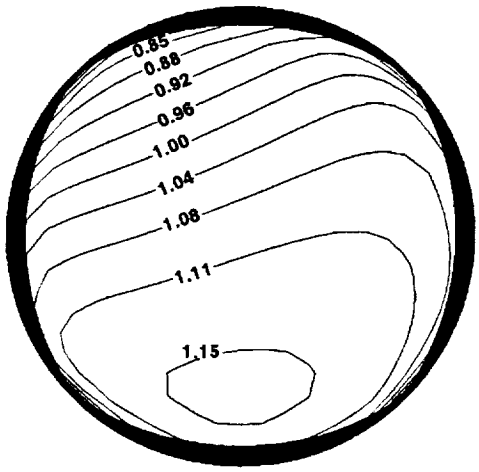

RP-1 Feedline CFD Results (MSFC's Design)

Nondimensionalized Axial Velocity

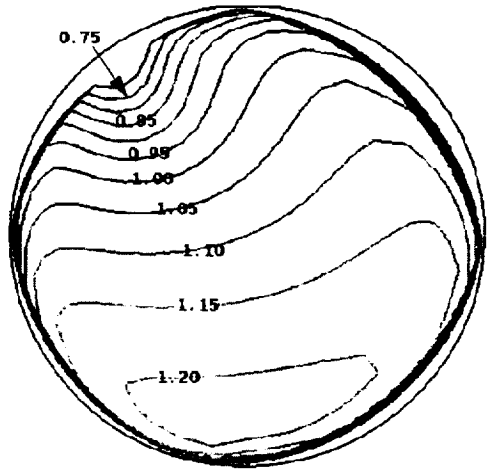

Figure 7: Engine Interface Velocity Contours

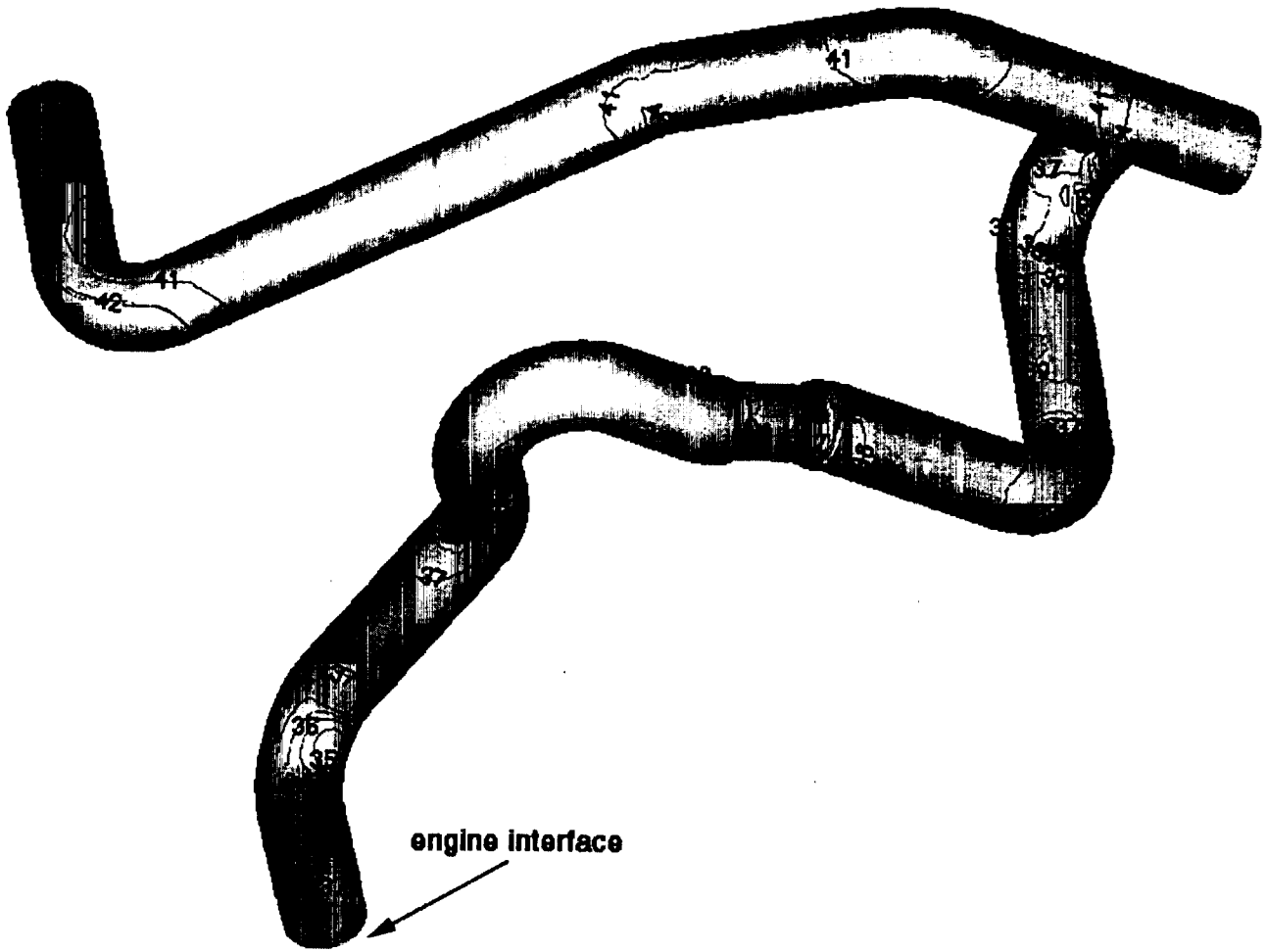

Figure 8: Static Pressure on RP-1 Feedline Walls

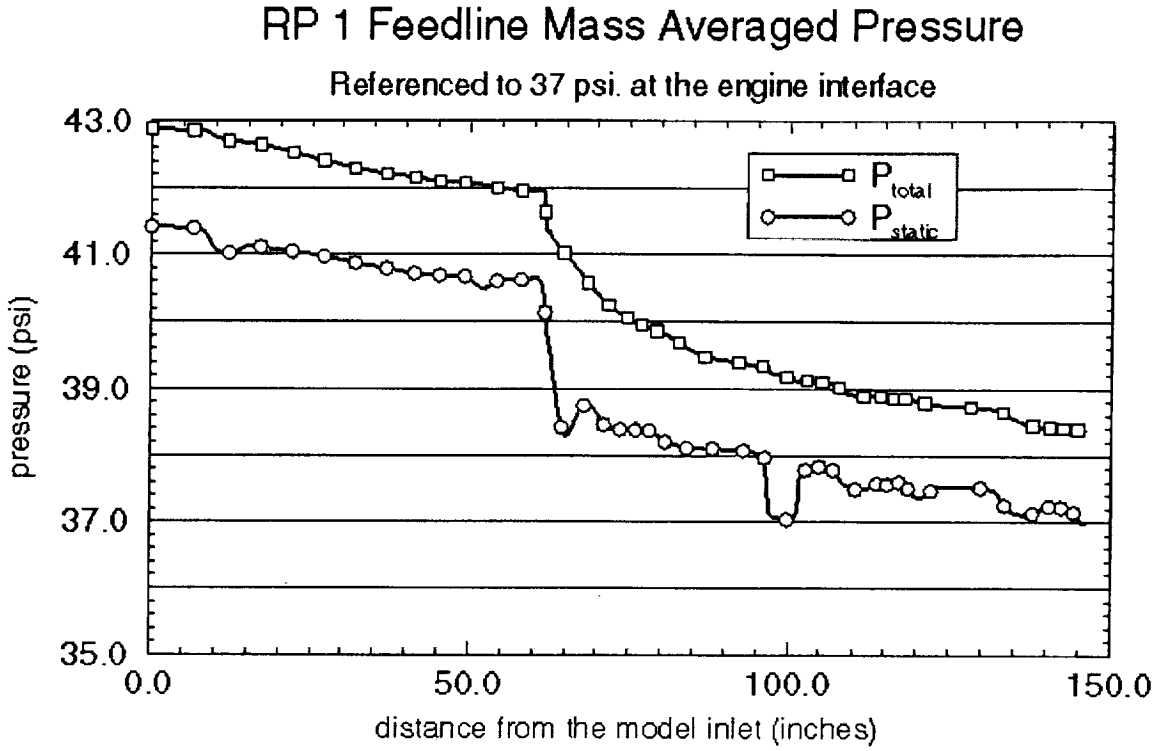

Figure 9: RP-1 Feedline Mass-Averaged Pressure Distribution

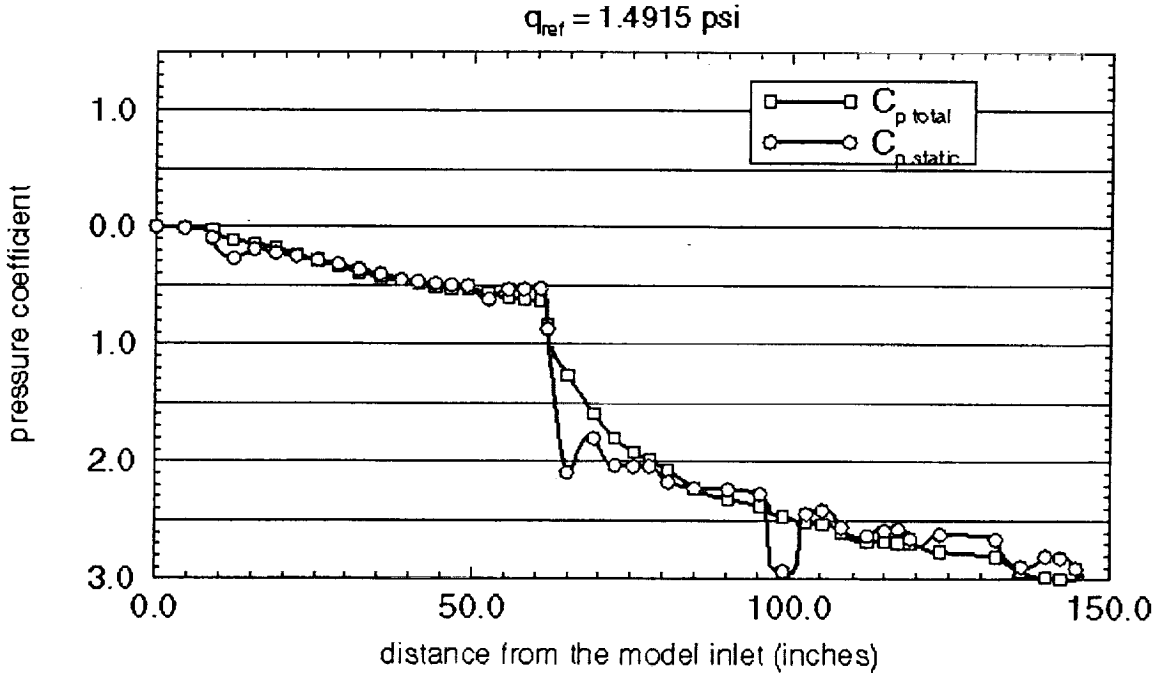

Figure 10: RP-1 Feedline Mass-Averaged Pressure Coefficient Distribution